Enhanced tribological properties of copper metal-matrix composites reinforced with fluorinated graphene oxide nanosheets

Nicky Savjani[a]*, Vicente Orts Mercadillo*[a]*, Darren Hodgeman*[b]*, Yubao Deng*[a]*, Cristina Vallés*[a]*, Mark A. Bissett*[a*] *and Ian A. Kinloch*[a]*

[a] Department of Materials, Henry Royce Institute and National Graphene Institute, The University of Manchester, Oxford Road, M13 9PL, UK.

[b] Carbon Science Center of Excellence, Morgan Advanced Materials and Technology, Inc., 310 Innovation Boulevard, Technology Center, Suite 250, University Park, PA 16803, USA.

Abstract. Applications of copper coatings on metal components are abundant owing to their high conductivities, corrosion resistance and anti-bacterial properties. However, applications of these coatings on moving parts are limited due to their poor tribological properties; tendencies to generate high friction and susceptibility to degradative wear. In this study, we have fabricated a fluorinated graphene oxide-copper metal matrix composite (FGO-CMMC) on a bearing steel substrate by a simple electrodeposition process in water. The FGO-CMMC coatings exhibited excellent lubrication performance under pin-on-disk (PoD) tribological sliding, which reduced CoF by 63 and 69%, compared to the GO-CMMC and pure copper coatings that were also prepared. The lubrication enhancement of the FGO-CMMCs is attributed to the tribochemical reaction of FGO with the AISI 52100 steel counterface initiated by sliding load. The formation of an asymmetric tribofilm structure on the sliding track is critical; the performance of the FGO/Cu tribofilm formed in the track is boosted by the continued fluorination of the counterface surface during PoD sliding, passivating the tribosystem from adhesion-driven breakdown. Other influences include the improved interlaminar shear strength of the FGO-containing composite. The excellent lubrication performance of copper coatings by FGO incorporation makes the CMMC a promising solid lubricant candidate for use in mechanical engineering applications.

Keywords: fluorographene, copper metal-matrix composite, solid lubrication, tribology, tribochemistry.

1. Introduction

Mechanical friction is the ubiquitous force that resists motion when two mutually contacting surfaces are moved relative to each other.[1] Approximately 23% of the world's energy consumption is lost to friction.[2] Minimizing friction would also reduce wear failures within mechanical systems in addition to improving energy efficiencies and lowering their environmental impact.

Copper-coating of mechanical components and surfaces is commonplace in industry[3] due to the coatings' excellent chemical and physical properties imparted onto the surface of a component. These include; its high thermoelectrical conductivities, corrosion resistance and antimicrobial properties.[4-7] However, the application of copper coatings within contact mechanisms is somewhat limited due to its poor wear resistance under applied load.[8] Therefore, improving the anti-wear ability of copper has become a key issue for use in high-performance mechanical components.

Lamellar materials such as graphite have been extensively used as solid lubricants over the last 60 years.[9] As a popular solid lubricant, graphite possesses many attractive features; excellent mechanical properties, low friction coefficient from its low anisotropic shear strength and good wear resistance.[10] Its two-dimensional analogue, graphene,[11] have shown significant promise in ultralow friction in both nanoscale and microscale lubrication,[12-15] supported by *in silico* measurements.[16-18] The materials' extremely high strength, low shear resistance, relatively low cost and comparably high thermal conduction and dissipation performances are attributed to the materials' 2D-lamellar structures.[19-21] More recently a fluorine-functionalised derivative, fluorographene, has been explored as a potential candidate for macroscale low-friction lubrication.[22, 23] Theoretically, the chemical and physical structures of fluorographenes should provide a route to ultralow friction. However, this has not been borne out experimentally,[24-26] as increased defect generation during fluorination increased the nanomaterials' shear strengths in macroscale sliding.

The development of advanced self-lubricating materials and coatings is a potentially promising approach for improving frictional and wear properties in surface engineering[27, 28] and is a target to replace grease-, oil-[29] and noble-metal[30, 31] lubricated systems within high-load, low-temperature mechanisms. Copper-metal matrix composites (CMMCs) could serve as the frictional material in electrical sliding contacts, such as brushes, bearing bushings and contact wires,[32-34] due to excellent thermal and electrical properties, as well as to expand into new horizons, including incorporation into high-speed transport and aerospace mechanisms.[35] The inclusion of graphene into CMMCs[32-34] has been proposed to enhance the desired mechanical functionalities of the metal, acting as second-phase reinforcement and as self-lubricating components within the composite.[36-43] Previous studies[41] have shown 1.1 wt.% RGO inclusion into an electrodeposited CMMC improves microhardness by ~ 30%. Furthermore, low graphitic loadings (sub-10 wt%) into copper films greatly diminish frictional losses under low contact pressure nano-and macrotribological testing.[44, 45, 21] Fluorographenes have been utilized in oil-based[46-49] and polymer-based[50-52] lubricating formulations. However, the incorporation of fluorographenes into metal composites have scarcely been explored.[53, 54]

It is still a challenge to homogeneously disperse graphenes in metal matrices with robust interfacial bonding due to the chemical inertness of each component, their varying wettabilities and thermal expansion coefficients, and difficulties in the uniform distribution of the nanomaterials.[55, 56, 21] By promoting good interfacial interactions between the components of CMMCs it is possible to improve its frictional performance. Therefore, improving the dispersibility and interaction parameters between graphene and copper is key to obtaining high tribological performance. Although some mechanisms such as copper-grain refinement and formation of tribofilms were proposed to explain the tribological behaviour of graphene–metal matrix composites,[57] the tribo-induced chemical reactions on the friction surfaces during a friction process are still unclear. In particular, the tribochemical information of graphene is needed to gain insight into the tribological mechanisms of the composite as a whole.

In this study, CMMCs containing fluorinated graphene oxide (FGO) were uniformly deposited onto bearing steel substrates by electrodeposition in water. These fluorinated graphene oxide-copper metal matrix composites (**FGO-CMMCs)** exhibited excellent macroscale lubrication properties, compared to graphene oxide (GO) containing CMMCs and pure copper coatings. The mechanism for the enhanced lubrication performance was also studied in detail.

2. Experimental Section

2.1. Materials:

A GO slurry was received from The Sixth Element (Changzhou) Materials Technology Co. Ltd. The slurry was frozen overnight before freeze-drying to produce a dehydrated powder, which was blended and sieved to < 50 μm. FGO was prepared using plasma-fluorination. The Haydale HT-60 lab scale reactor was used to process a 25g batch of material in a CF_4 plasma, at low temperatures (<100 °C) and pressures (<1 mbar). A detailed characterisation of the GO and FGO powders is provided in ESI (Figure S1-S3, Table S1).

The components of the nickel-Watts (nickel sulfate, nickel chloride and boric acid) and copper (Etidronic acid, copper(II) carbonate hydroxide, potassium pyrophosphate, sulfamic acid, potassium hydroxide and potassium carbamate) plating solutions were purchased from Sigma-Aldrich. All chemicals were used as supplied.

The nickel-Watts plating solution was produced as described elsewhere.[58] The alkaline copper-plating solution was modified from the cited recipe[59]: For a litre of the solution, basic copper carbonate (30 g) was initially dissolved in Etidronic acid (65 wt%; 150 g), and made up to 600 mL with deionized water, before the addition of sulfamic acid (50 g) and potassium pyrophosphate (100 g). The solution was raised to pH 6 by the slow addition of potassium hydroxide (~70 g); gelation occurs at pH 5, which redissolves at higher pH. Finally, potassium carbonate was added until a pH of 9 is obtained (~100 g).

FGO-Copper and **GO-Copper** plating dispersions were prepared by loading the basic copper plating solution with FGO or GO powders to achieve a 1 mg/mL dispersion, followed by ultrasonication for two hours (Elmasonic P70H, 37 kHz amplitude, 100% power) and storage. Before use, the dispersions were agitated by sonication for 15 minutes.

SKF LS-1528 (AISI 52100, 28mm OD, 15 mm ID, 2.75 mm thick) and LS-2542 (AISI 52100, 42 mm OD, 25 mm ID, 3.00 mm thick) raceway washers were purchased from shop.Eriks.co.uk. 8 mm diameter, 52100 ball bearings (Grade 10: Ra ≤ 25 nm) were purchased from Simplybearings.co.uk. Both the 52100 washers and ball bearings are used as supplied. The 52100 washers and ball bearings were cleaned before use by successive ultrasonic cleaning steps in isopropanol (twice) and acetone followed by freeboard drying. Once cleaned, the materials were seal-packed in LDPE bags until required. For thickness determination of a given coating, eight areas of the substrate were masked with latex before deposition: four along the inner edge and four on the outer edge of the 52100 washer (Figure S4).

2.2. Methods:

Electroplating of the **FGO-CMMC**, **GO-CMMC** and **$\mathbf{Cu_{Ref}}$** coatings onto the 52100 substrates was achieved using an electroplating assembly (Figure 1a). The assembly consisted of a 400 mL tall form Borosilicate glass beaker, with 200 mL of plating solution and a magnetic stirrer to ensure homogenous mixing during electroplating. Four Cu sheets (approx. 20 x 1 x 200 mm) were evenly spaced around the inside perimeter of the beaker and connected to act as the anode. The cathode was made from a masked AISI 52100 washer, suspended in the plating solution using Cu wire. The current density was controlled using a current-limited power supply (Agilent E3631A). To assist with uniform **FGO-CMMC** and **GO-CMMC** co-plating, a 100 nm nickel flash layer was deposited (Watts solution, 1 A/dm^2, 30 secs) onto the AISI 52100 washer before Cu-plating. After washing the Ni-flashed 52100 substrate with water and isopropanol, it was plated in the respective plating dispersions/solutions for **FGO-CMMC**, **GO-CMMC** and **$\mathbf{Cu_{Ref}}$** deposition experiments. The current density and deposition time were adjusted to achieve ~20 μm-thick coatings on the washer (0.25 A/dm^2 for 6 hours, or 3 hours at 0.5 A/dm^2). After completing a deposition, each coating was stored with silica gel to inhibit oxidation.

White light Interferometry measurements for **FGO-CMMC**, **GO-CMMC** and **Cu_{Ref}** coatings were undertaken using a Bruker Contour-GT white-light profilometer equipped with a 2.5x optical lens. The reported thickness of a given CMMC is based on the average thickness measured across each of the paired masked areas (Figure S4; Red markings). All surface roughness (R_a) measurements were also obtained by WL profilometry, from a ~9 mm2 area of the coating located at the same position on each sample (Figure S4; black markings).

The surfaces of the **FGO-CMMC**, **GO-CMMC** and **Cu_{Ref}** coatings were observed by scanning electron microscopy (SEM, Quanta-250 FEG-SEM) at 20 keV along with energy-dispersive spectroscopy (EDX, Xmax 80, Oxford instruments). The focal length for imaging and analysis was fixed at 10mm.

Grazing Incidence X-ray diffraction (GI-XRD) studies were performed using a Philips X'Pert–MPD theta-theta diffractometer (400 mm diameter) with a PW1711 (Proportional) point detector in Bragg-Brentano geometry employing a Copper Line Focus X-ray tube with Ni k_{β} absorber (0.02 mm; $K\beta$ = 1.392250 Å) $K\alpha$ radiation ($K\alpha_1$=1.540598 Å, $K\alpha_2$=1.544426 Å, $K\alpha$ ratio 0.5, $K\alpha_{av}$=1.541874 Å). Incident beam Soller slit of 0.04 rad, incident beam mask 10 mm, programmable automated divergence slit giving a constant illuminated length of 10.0 mm, programmable anti-scatter slit observed length of 10.0 mm, receiving Soller slit of 0.04 rad, Parallel plate collimator (0.27°) and diffracted beam curved graphite monochromator (002). Data collection from 3 to 90° 2θ scan at 0.02° step size and 4 s/step was undertaken.

Raman spectroscopy was carried out in a Renishaw inVia Raman Spectrometer using a laser excitation wavelength of 514 nm at 100x magnification, operating at approx. 1 mW. The spectra were acquired through a spectrum window of 250-3500 cm^{-1}. In all experiments, the 52100 substrate does not contribute to any signals within the observed Raman spectral window.

Microindentation experiments were carried out using a CSM Micro Indentation tester equipped with a Vickers diamond tip. All indentations were carried out with a 5N load for direct comparison.

Reciprocating pin-on-disk (PoD) sliding tests were performed on a Bruker UMT Tribolab tribometer with a 1-100N load cell installed. The data sample rate of 1,000 Hz was selected. The CoF trace (μ) is obtained by first processing the applied load (F_z) and frictional force (F_x) traces to generate an F_x/F_z trace. To remove datapoints attributed to static (and quasi-static) friction modes, the value for μ for each stroke (= 0.5 Hz) is taken from the average of the middle 50% of the F_x/F_z trace as this represents the dynamic friction phase of the sliding tests.

3. Results and Discussion

3.1. Coating fabrication and characterisation

Three sets of coatings were prepared by electrodeposition of the respective graphene-copper plating dispersions onto AISI 52100 steel washers (Figure 1a); FGO- and GO-containing copper coatings onto AISI 52100 (**FGO-CMMC** and **GO-CMMC**), alongside graphene-free copper coatings (**Cu$_{Ref}$**) for comparison. For each set of coatings, the effect of deposition power was further studied by preparing coatings at two current densities (0.25 and 0.5 A/dm^2).

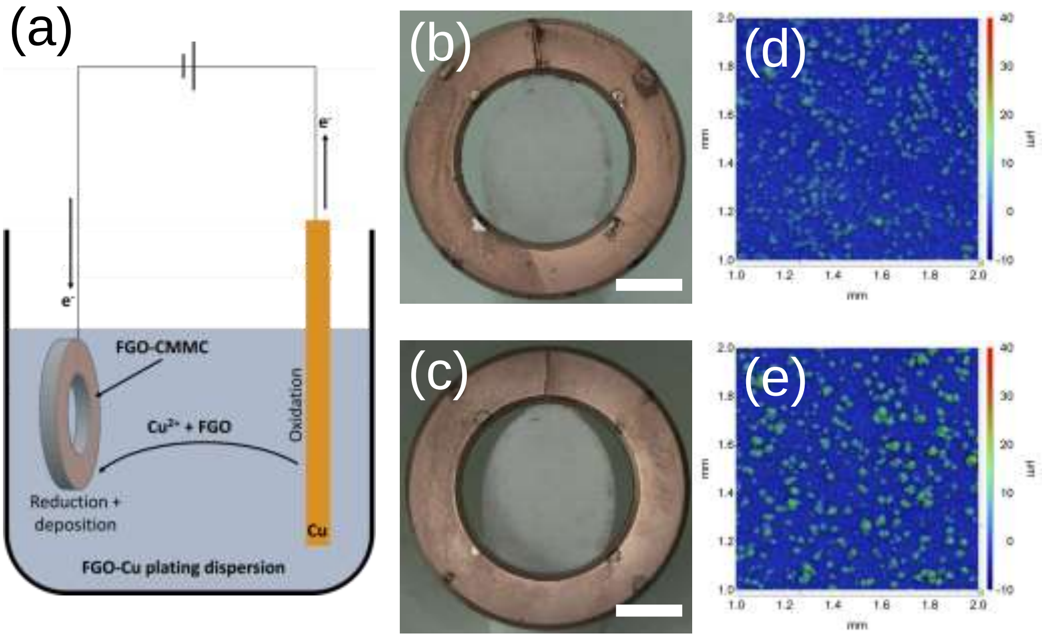

Figure 1. Preparation of the **FGO-CMMC** coatings on AISI 52100 steel. (a) Schematic of the electrodeposition process. (b, c) Photographs of the coatings prepared at a current density of b) 0.25 A/dm^2 (**FGO-CMMC$_{(0.25CD)}$**) and c) 0.5 A/dm^2 (**FGO-CMMC$_{(0.5CD)}$**). The scale bars on the photographs indicate 10 mm. (d, e) WL interferometry topographs of the coatings from b) and c.).

FGO-CMMC coatings were uniformly deposited onto steel washers (Figure 1b, c). The equivalent **GO-CMMC** and **Cu$_{Ref}$** coatings were also produced as ascribed in detail in ESI (Figure S6). Thicknesses of the **FGO-CMMCs** prepared at 0.25 and 0.5 A/dm^2 were 18.4

and 18.3 μm, respectively, close to the 20 μm thicknesses targeted for the project (Figure S5). The surface morphology of the **FGO-CMMC, GO-CMMC** and **$\mathbf{Cu_{Ref}}$** coatings was assessed by white light (WL) interferometry and SEM. It can be observed that **FGO-CMMC** and **GO-CMMC** coatings have a similar topography across the whole substrate; the surface of the coating is mostly level but is perturbed by a significant number of additional growths that protrude over the level-plated surface (Figure 1d, e). The sizes of these growths range from a few microns to up to ~60 μm. Often, FGO and GO nanosheets are found embedded inside these growths protruding from its core, as identified by SEM imaging (Figure 2a-d, ESI Figure S6i, j, m, n). All nanosheets identified within the composites showed no copper nanoparticle growth on their surface, suggesting the graphitic sheets are anchored into the Cu coating only by edge interactions before further coating growth captures the nanosheets within the copper heterophase. WL interferometry topographs show that **FGO-CMMC** coatings show higher coverage of these growths on the plated surface (~40-50% in a 3.75 mm^2 area, versus ~10% for **GO-CMMCs**), however, the footprint of these growths on the **GO-CMMC** coatings are significantly larger (Table S3). This may suggest that FGO can co-deposit with copper more uniformly and without aggregation, compared to GO incorporation. As a consequence, the R_a values of these coatings have increased to > 1 μm (*c.f.* <300 nm for **$\mathbf{Cu_{Ref}}$**).

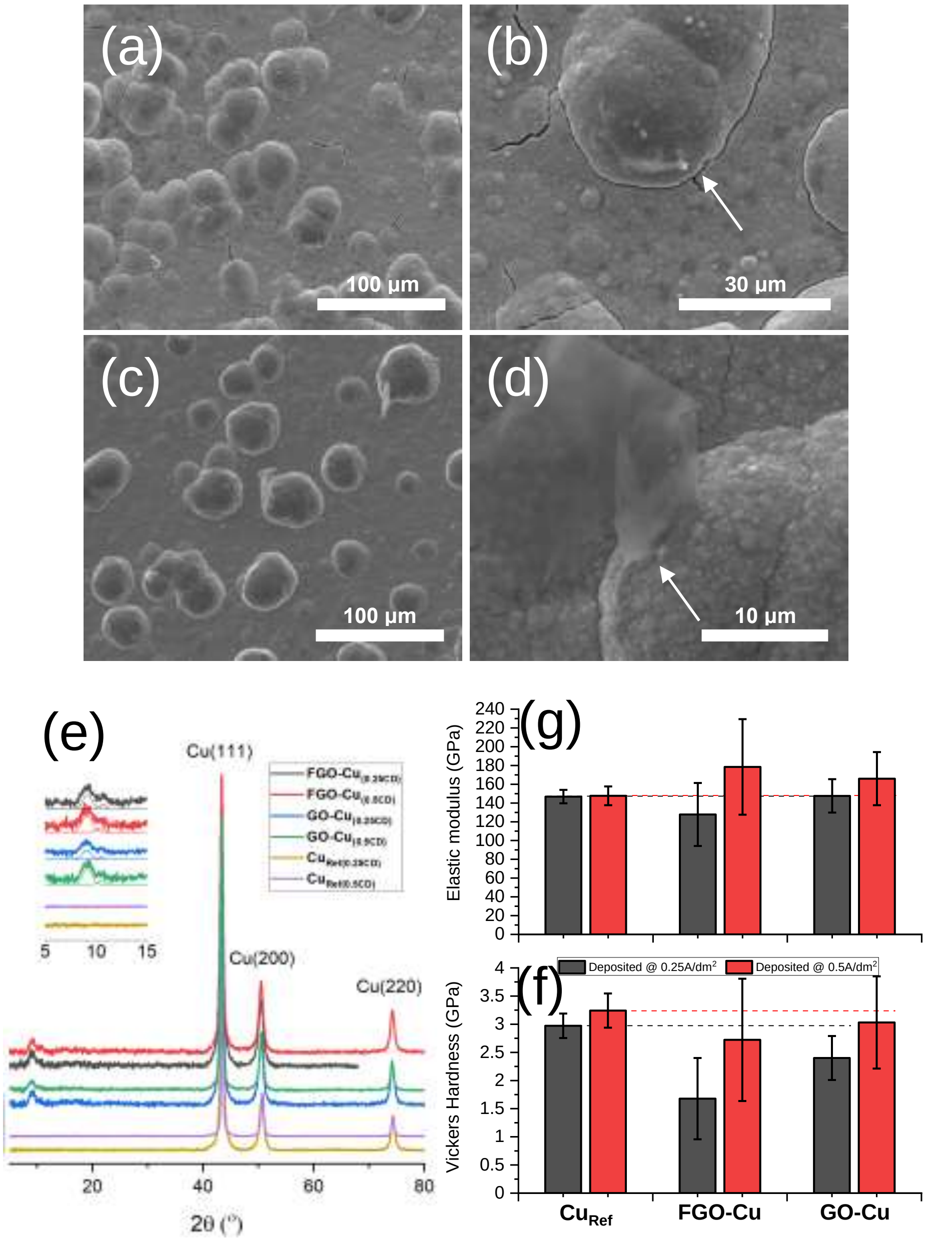

Figure 2. Physical and spectroscopic characterisation of CMMC coatings on AISI 52100 steel: Scanning electron microscopy (SEM) images of the coatings: (a) **FGO-CMMC$_{\mathbf{(0.25CD)}}$** (c) **FGO-CMMC$_{\mathbf{(0.5CD)}}$**, (b and d) are magnified sections of a, c), highlighting the capture of FGO within the coating structure. (e) X-ray diffractograms of all **FGO-CMMC**, **GO-CMMC** and **Cu$_{\mathbf{Ref}}$** coatings; insert expands on the FGO and GO peaks observed within the composite coatings. (f) Vickers microhardness and (g) reduced elastic moduli of the **FGO-CMMC**, **GO-CMMC** and **Cu$_{\mathbf{Ref}}$** coatings, values were obtained from an average of 49 microindentations.

XRD studies reveal information on the microcrystalline nature of the CMMCs produced by co-deposition with graphene (Figure 2e). The 0.25 and 0.5 A/dm^2 coatings are compared to their equivalent **Cu$_{\mathbf{Ref}}$** coatings. All coatings show a pattern consistent with pure copper (fcc) with no evidence of lattice strain induced by graphene incorporation.[60] The Ni flash layer is absent due to its thinness and amorphous nature. The **FGO-CMMC** and **GO-CMMC** coatings display a small diffraction peak at ~9° relating to the (001) diffraction of (F)GO nanosheets within the coating. This can be further deconvoluted into two peaks, as shown in the figure inset, indicative of two crystallographic phases: The dominant peak (at 9.3° and 9.1°) corresponds to restacked FGO and GO with an increased interlayer spacing (9.7 and 9.3 Å), while the weaker peak (at 10.9° and 10.8°) corresponds to more tightly packed native FGO and GO (8.2 and 8.0 Å). The latter values are representative of the (001)-stacking of FGO and GO powders characterised in the ESI (Figure S1). In all cases, the relative intensity of the graphitic peaks to the Cu pattern is consistent, suggestive of a similar graphitic concentration within the CMMCs.

The co-deposition of (F)GO into CMMCs has a significant effect on their mechanical properties (Figure 2f and g). **FGO-CMMC$_{\mathbf{(0.25CD)}}$** shows the most pronounced effects, as its hardness (1.67 GPa) is considerably lower than for both **Cu$_{\mathbf{Ref(0.25CD)}}$** and **GO-CMMC$_{\mathbf{(0.25CD)}}$** (2.97 and 2.39 GPa). This accounts for ~43 and 18% reduction in hardness for the copper coating upon FGO and GO incorporation when deposited at 0.25 A/dm^2. This results in a coating that has lower elasticity and higher ductility – desired properties in solid lubrication systems facilitated by soft metals.[61] Less significant reductions in *H* values were reported when deposited at 0.5 A/dm^2, with values of 2.72, 3.03 and 3.24 GPa for **FGO-CMMC$_{\mathbf{(0.5CD)}}$,** **GO-CMMC$_{\mathbf{(0.5CD)}}$** and **Cu$_{\mathbf{Ref(0.5CD)}}$** coatings, confirming a 16 and 7% reduction in hardness of the copper coatings by FGO and GO incorporation. The elastic moduli of all **FGO-CMMC** and **GO-CMMC** are (within error) consistent with observed values for their **Cu$_{\mathbf{Ref}}$**

counterparts, albeit with a higher degree of deviation as a cause of the rougher surfaces from graphene incorporation.

3.2. Mechanism for FGO-CMMC and GO-CMMC co-deposition

A detailed chemical analysis of the FGO and GO powders and filtrates (post-dispersion in the copper plating solution) is provided in the ESI. Alongside the information obtained on the coatings, a mechanism for the deposition of **FGO-CMMCs** and **GO-CMMC**s onto AISI 52100 steel can be tentatively proposed (Figure 3). The example below focuses on the use of GO within the mechanism for clarity but can also be interpreted for FGO inclusion. Evidence from XRD, Attenuated total reflectance-Fourier transform infrared (ATR-FTIR) spectroscopy and X-ray photoelectron spectroscopy (XPS) shows that in the production of the plating dispersion, the carboxylic acid groups on (F)GO nanosheets are functionalized by a K^+ salt in the solution, resulting in an edge-functionalised nanosheet. The nature of the ion functionalisation is not clear, but XPS evidence suggests that a form of $(K^+)_x(CO_3)_x$ is present. The functionalisation of the graphitic nanosheets also aids in stabilising the plating dispersion to aggregation. During deposition, the metallic moieties on the functionalized graphenes anchor to the growing copper film by edge interactions. With continued growth, the GO nanosheet binds to the growing copper film in a passive manner. There is no further chemical activation of the nanosheet surface (namely at the alkoxy/epoxy sites), inhibiting any CuNP nucleation on its surface. The binding interface between Cu and the nanosheets may induce a nucleation site for further copper growth, growing misorientated grains that embed the nanosheet within the film.

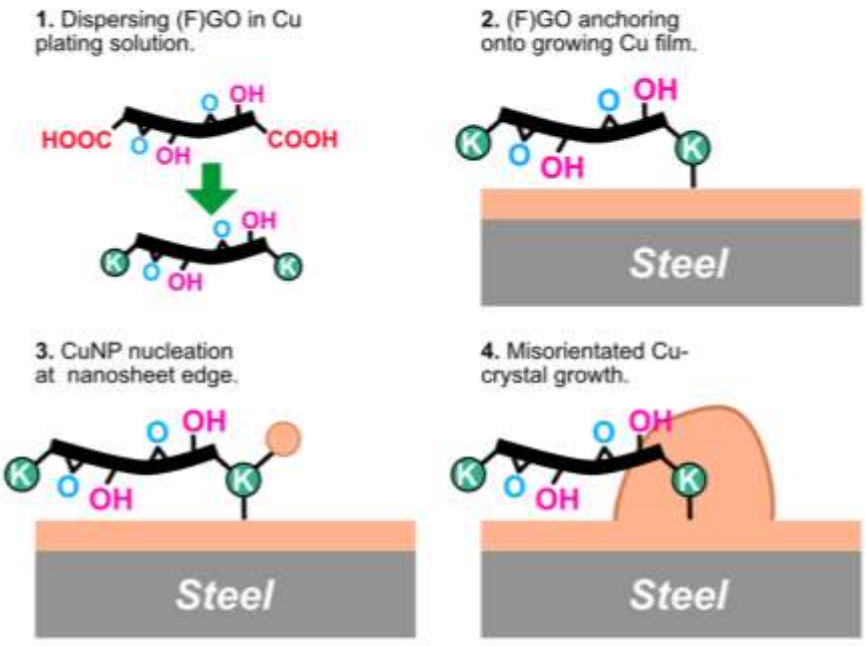

Figure 3. The postulated mechanism for the co-deposition of **FGO-CMMCs** and **GO-CMMCs** on AISI 52100 steel.

3.3. Tribological testing

3.3.1. Friction

The coefficient of friction (CoF; μ) of the CMMCs was measured by reciprocating Pin-on-Disc (PoD) sliding in ~40% RH, under a normal load of 1 N (~320 MPa Hertzian contact pressure) selected to attempt to prolong the low-friction phase in the early phases of testing. **Cu$_{\mathbf{Ref}}$** coatings typically show a rapid increase of friction after run-in, achieving $\mu > 0.3$ in less than 500 revs and stabilising at ~0.6 until testing was stopped at 10,000 revs (Figure 4a). **GO-CMMC** gave tentative performances as a low-friction lubricating surface. Both **GO-CMMC$_{\mathbf{(0.25CD)}}$** and **GO-CMMC$_{\mathbf{(0.5CD)}}$** achieve a near-immediate low-friction sliding ($\mu \leq 0.2$) for a short period (approx. 750 revs), before lubrication fails and unstable, high-friction sliding modes are observed. In contrast, **FGO-CMMC** coatings show superior friction throughout the test period; a near-instant low-friction regime was observed at the start of **FGO-CMMC** $_{(0.25CD)}$, sliding, and μ remained below 0.2 until tests were stopped at 10,000 revs of sliding (Figure 4b). **FGO-CMMC** $_{(0.5CD)}$ displays similar low-friction running at the start of the sliding tests, but its performance fatigues after ~4,300 revs, followed by a slow rate of μ increase to ~0.25 by the end of testing.

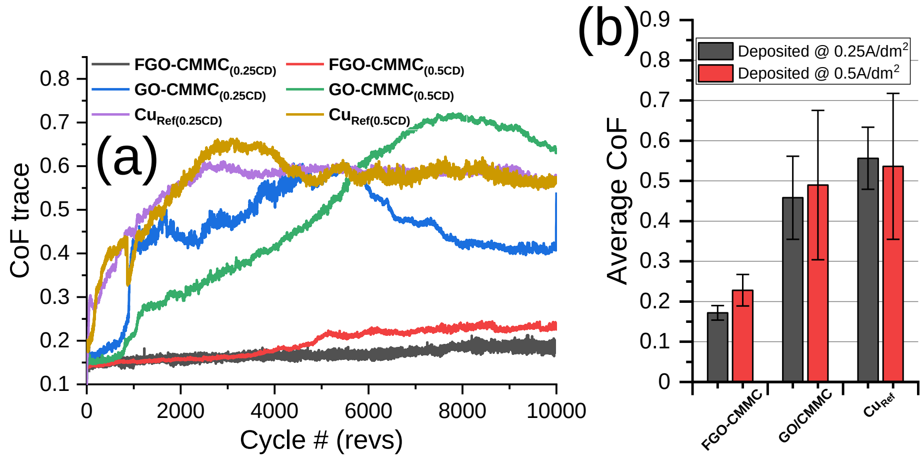

Figure 4. (a) Reciprocating PoD friction traces for **FGO-CMMC**, **GO-CMMC** and **Cu**$_{\text{Ref}}$ coatings. The bar chart in (b) is the average CoF calculated from the whole CoF trace for each sample run.

The sliding tests conclude that the incorporation of graphene oxide into a copper composite can generate a low-friction sliding surface. However, the longevity of the low-friction phase is owed to the function of the fluorinated groups in FGO.

3.3.2. Wear

To reveal the lubrication and antiwear mechanisms of the CMMCs, the morphology of the wear track after sliding friction tests was analyzed by WL interferometry and SEM.

Optical and WL imaging on the sliding tracks on both **FGO-CMMC**$_{(0.25CD)}$ and **FGO-CMMC**$_{(0.5CD)}$ show that wear is limited to the top of the protruding misorientated growths, limiting the contact area on the coating; the high populous for these growths ensure that counterface-sliding does not contact the bulk copper coating (Figure 5). Observed wear depths after 10,000 revs sliding are limited to < 5 μm, suggesting that the coatings can achieve a low-friction regime beyond the 10,000 revs endpoint selected. SEM imaging of the wear surface on **FGO-CMMC$_{\mathbf{(0.25CD)}}$** showed clear evidence of shear-delamination: the contact surfaces are smooth, with the debris primarily consisting of platelet-structured materials. EDX mapping shows that the sliding contact surfaces are rich in carbon but contains no-enriched fluorine content. The debris surrounding the contact areas was also found to contain carbon and oxygen, suggesting that the ejected debris is from the oxidized FGO-Cu tribofilm. In contrast, **FGO-CMMC$_{\mathbf{(0.5CD)}}$**, which showed a partial failure of low-friction running at 4,300 revs, observed surface fatigue of the contact areas in the form of pitting and coating delamination, accompanied by the redistribution of larger particles around the contact surfaces from the erosion of the sliding surface. This is commensurate to small increases in interlayer shear energy, accompanied by susceptibility to oxidation at higher levels of friction.

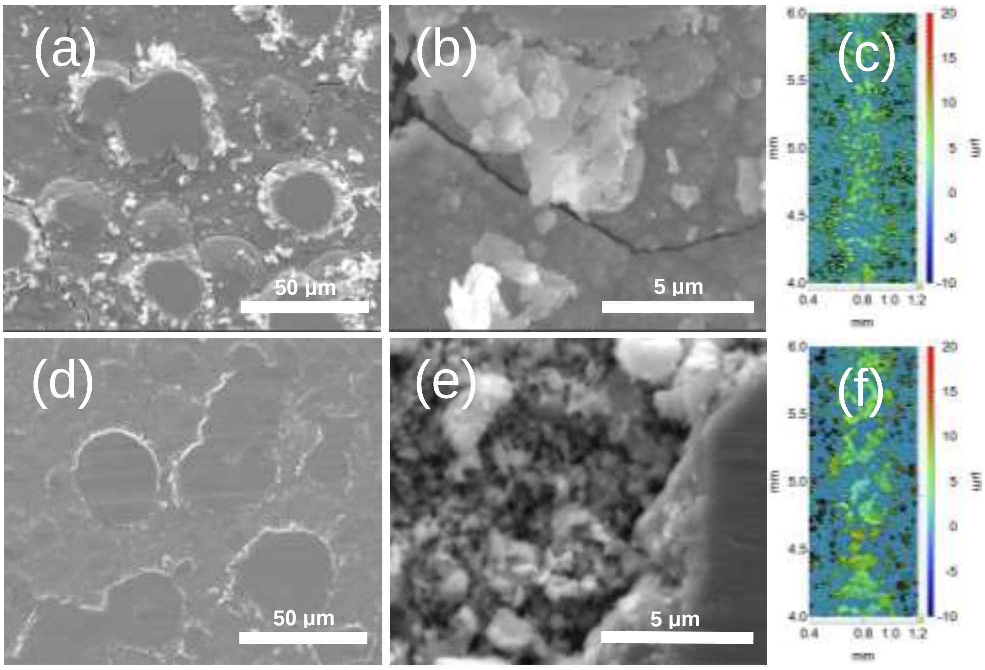

Figure 5. Imaging of the wear scars on **FGO-CMMC** coatings. SEM imaging of the wear on (a, b) **FGO-CMMC$_{(0.25CD)}$** (d, e) **FGO-CMMC$_{(0.5CD)}$**, identifying the wear tracks and debris generated from sliding testing. (c, f) WL interferometry topographs of the wear scars show no penetration into the bulk of the coating.

The ~9,000 rev high-friction sliding observed during PoD testing of **GO-CMMC$_{(0.25CD)}$** and **GO-CMMC$_{(0.5CD)}$** is evident in post-test wear scar analysis, as the misaligned growths on these coatings have a significantly higher degree of abrasive wear when compared to **FGO-CMMC** (Figure S8). More so, the concentration of misaligned crystal growth on the surface dictates the depth of wear observed. The **GO-CMMC$_{(0.5CD)}$** sliding track predominantly shows high wear of the embedded growths, but limited penetration into the Cu-bulk coating. **GO-CMMC$_{(0.25CD)}$**, on the other hand, shows penetration into the bulk-copper surface. GO-CMMCs succumb to wear of the bulk coating as a consequence of the lower area coverage of such growths on its surface (~ 10% of the surface area, *c.f.* > 40% for FGO-CMMCs; Table S3). It is also noted that the high μ observed has given rise to coating fracturing, delamination and erosion, resulting in microparticle-type debris redistributing along the sliding track. This was also observed after sliding on **Cu$_{\mathbf{Ref}}$** coatings (Figure S7). The high-friction running on the coating is also anticipated to inhibit the formation of a robust tribofilm on the sliding track, as shown by the lack of surface carbon in the EDX map (Figure S8).

To further aid understanding, the morphology and elemental distributions of the AISI 52100 counterface ball from **FGO-CMMC$_{\mathbf{(0.25CD)}}$** sliding were investigated by SEM and EDX (Figure 5). The SEM image of the counterface shows that the contact area has suffered minimal damage, as the topography and roughness have not increased significantly (*c.f.* counterfaces from **GO-CMMC$_{\mathbf{(0.25CD)}}$** and **Cu$_{\mathbf{Ref(0.25CD)}}$**, sliding; Figure S8). Raman analysis of the contact area shows no evidence of typical graphitic bands at 1360 and 1680 cm^{-1}, indicating no graphene-based transfer films are formed. Moreover, EDX maps of C, Cu and F confirm that the counterface contains minimal copper and carbon on the surface, but its surface is fluorine-rich. The formation of the fluorinated steel surface is consistent with a tribochemical reaction between FGO and steel under a sliding load.

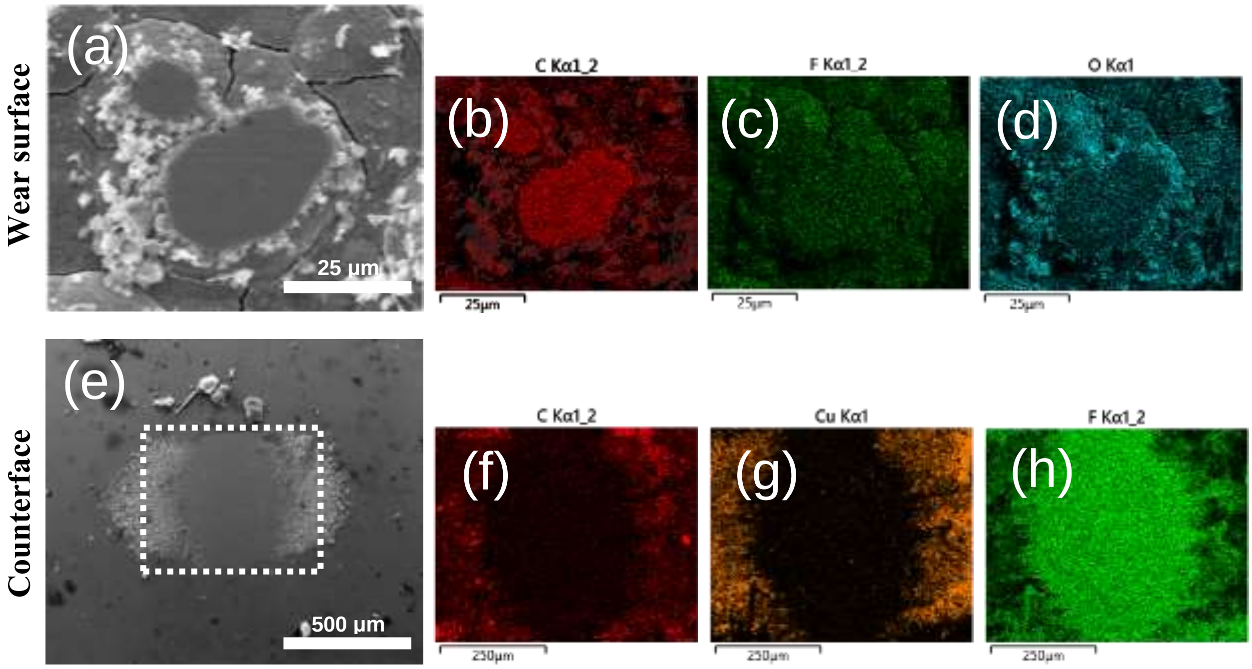

Figure 6. (a) SEM imaging and (b-d) EDX elemental mapping of a wear surface formed on **FGO-CMMC$_{\mathbf{(0.25CD)}}$** after PoD sliding for 10,000 revs. (e) An SEM image of the wear surface on the AISI 52100 counterface after PoD sliding on **FGO-CMMC$_{\mathbf{(0.25CD)}}$**, (f-h) accompanied by elemental maps obtained by EDX analysis

3.4. The lubrication mechanism of FGO-CMMC and GO-CMMC coatings.

The macroscale low-friction performance of **FGO-CMMCs** and **GO-CMMCs** is driven by the sliding interface between the graphene-copper tribofilm and the steel counterface, but low-friction lifetimes and antiwear performances are influenced by the formation of a robust fluorine-rich transfer layer on the counterface. Graphene is known to not easily form a tribolayer onto steel surfaces due to its chemical inertness.[62] Conversely, the oxygen-functional groups on graphene oxide are susceptible to adhesion onto metal surfaces,[63] as well as inhibiting low-shear interactions between nanosheets, therefore, accelerating damage of the nanosheets under sliding. Liu *et al.*[23] recently demonstrated that sliding fluorographene oxide coatings on steel generates a metal-fluoride surface on the steel counterface, promoting a robust transfer film[64] that facilitates a low-shear sliding mechanism between steel contact pairs. However, due to the nature of the contact pair in **FGO-CMMC** sliding, there is no evidence of carbon on the transfer film, suggesting that the tribofilm structure is asymmetric: the coating reconstructs under sliding load to a lamellar FGO/Cu tribofilm, sliding against the fluorine-passivated steel counterface, it is this structure that provides the long-lasting, low-friction performance (Figure 7). This is beneficial for low-friction longevity as the fluorine-rich transfer film is continually regenerated by the gradual wear and reconstruction of the FGO/Cu tribofilm, further retarding coating failure. Secondary effects of **FGO-CMMC** lubrication include the improved ductility of the composite (*c.f.* pure copper) that further reduces the coatings' macroscale interlaminar shear strengths, allowing for a more efficient construction and maintenance of the tribofilm during sliding.

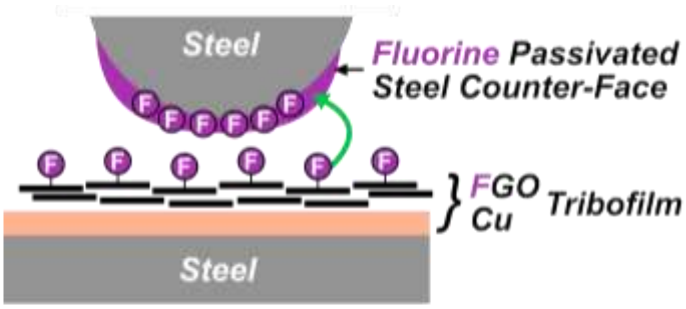

Figure 7. A schematic representation of the asymmetric tribofilm formation upon PoD sliding on **FGO-CMMC** coatings.

The FGO within the CMMC forms a robust tribofilm on steels that exhibits excellent low-friction and antiwear properties. Therefore, the **FGO-CMMC** is a promising solid lubricant for mechanical engineering applications.

4. Conclusions

Low-profile **FGO-CMMC** coatings were uniformly deposited onto bearing steels by electrodeposition and exhibited excellent lubrication performances under macroscale sliding, reducing the average CoF by 69 and 63% over an extended test period, compared to coatings of pure copper and **GO-CMMC** with similar topography. The improved lubrication performance and wear resistance of the FGO-containing CMMCs than those with GO was attributed to the construction of a robust, asymmetrically structured sliding tribofilm that promotes low-friction sliding and reduced wear. Other factors include improved ductility and reduced interlaminar shear strength of the copper coating upon FGO incorporation contributing to the excellent properties observed. The ease of **FGO-CMMC** composite deposition, combined with its excellent lubrication performance and wear resistance make it a promising solid lubricant for applications within engineering mechanisms.

Supporting Information

Full characterization of the GO and FGO powders, chemical characterization of the **$\mathbf{GO_{(filtrate)}}$** and **$\mathbf{FGO_{(filtrate)}}$** extracted nanosheets characterization of the as-prepared **GO-CMMC** and **$\mathbf{Cu_{Ref}}$** coatings and post-wear analyses on **GO-CMMC** and **$\mathbf{Cu_{Ref}}$** coatings are available on the ACS website.

Corresponding Author

E-mails: mark.bissett@manchester.ac.uk and ian.kinloch@manchester.ac.uk

Author Contributions

The manuscript was written through the contributions of all authors. All authors have approved the final version of the manuscript.

Acknowledgements

NS, MAB and IAK would like to thank the EU Graphene Flagship Core 3 (Grant Number 881603) for funding this work. VO acknowledges the Graphene NOWNANO CDT, and industrial sponsors Haydale Ltd. DH would like to acknowledge Morgan Advanced Materials as an employer during this work. IAK and CV would like to acknowledge the Royal Academy of Engineering and Morgan Advanced Materials.

Tribological assessments and XPS measurements were supported by the Henry Royce Institute for Advanced Materials, funded through EPSRC grants EP/R00661X/1, EP/S019367/1, EP/P025021/1 and EP/P025498/1. The authors thank the staff in the Department of Materials XRD Facility in the Faculty of Science and Engineering for their assistance.

References

1. Robertson, W. L., *Lubrication in Practice*. CRC Press: Boca Raton, FL, USA, 2019.

2. Holmberg, K.; Erdemir, A., Influence of Tribology on Global Energy Consumption, Costs and Emissions. *Friction* **2017,** *5* (3), 263. DOI: 10.1007/s40544-017-0183-5.

3. Jiang, Q.*, et al.*, A Review on Additive Manufacturing of Pure Copper. *Coatings* **2021,** *11* (6), 740. DOI: 10.3390/coatings11060740.

4. Chyderiotis, S.*, et al.*, New Insights on Antimicrobial Efficacy of Copper Surfaces in the Healthcare Environment: a Systematic Review. *Clin. Microbiol. Infec.* **2018,** *24* (11), 1130. DOI: 10.1016/j.cmi.2018.03.034.

5. Ikeshoji, T.-T.*, et al.*, Selective Laser Melting of Pure Copper. *JOM* **2018,** *70* (3), 396. DOI: 10.1007/s11837-017-2695-x.

6. Colopi, M.; Demir, A. G.; Caprio, L.; Previtali, B., Limits and Solutions in Processing Pure Cu *via* Selective Laser Melting Using a High-Power Single-Mode Fiber Laser. *Int. J. Adv. Manuf. Technol.* **2019,** *104* (5), 2473. DOI: 10.1007/s00170-019-04015-3.

7. Jadhav, S. D., *et al.*, Laser Powder Bed Fusion Additive Manufacturing of Highly Conductive Parts Made of Optically Absorptive Carburized CuCr1 Powder. *Mater. Des.* **2021,** *198*, 109369. DOI: 10.1016/j.matdes.2020.109369.

8. Yiran, W., *et al.*, Review of Preparation and Application of Copper–Steel Bimetal Composites. *Emerg. Mater. Res.* **2019,** *8* (4), 538. DOI: 10.1680/jemmr.17.00008.

9. Sliney, H. E. *Document 19910013083 - Solid Lubricants*; 19910013083; NASA Lewis Research Center: Cleveland, OH, 1991; (accessed 2022-06-15).

10. Liang, H.; Bu, Y.; Zhang, J., Graphene Oxide Film as Solid Lubricant. *ACS Appl. Mater. Inter.* **2013,** *5* (13), 6369. DOI: 10.1021/am401495y.

11. Ferrari, A. C., *et al.*, Science and Technology Roadmap for Graphene, Related Two-Dimensional Crystals and Hybrid Systems. *Nanoscale* **2015,** *7* (11), 4598. DOI: 10.1039/C4NR01600A.

12. Martin, J. M., *et al.*, Superlubricity of MoS2: Crystal Orientation Mechanisms. *Surf. Coat. Technol.* **1994,** *68-69*, 427. DOI: 10.1016/0257-8972(94)90197-x.

13. Oviedo, J. P., *et al.*, *In Situ* TEM Characterization of Shear-Stress-Induced Interlayer Sliding in the Cross Section View of Molybdenum Disulfide. *ACS Nano* **2015,** *9* (2), 1543. DOI: 10.1021/nn506052d.

14. Li, H., *et al.*, Superlubricity between MoS_2 Monolayers. *Adv. Mater.* **2017,** *29* (27), 1701474. DOI: 10.1002/adma.201701474.

15. Huang, Y.; Liu, L.; Yang, J.; Chen, Y., Nanotribological Properties of ALD-Made Ultrathin MoS_2 Influenced by Film Thickness and Scanning Velocity. *Langmuir* **2019,** *35* (10), 3651. DOI: 10.1021/acs.langmuir.8b03970.

16. Claerbout, V. E. P.; Polcar, T.; Nicolini, P., Superlubricity Achieved for Commensurate Sliding: MoS_2 Frictional Anisotropy *in Silico*. *Comp. Mater. Sci.* **2019,** *163*, 17. DOI: 10.1016/j.commatsci.2019.03.019.

17. Miura, K., Superlubricity of MoS_2 at Submicron Scale. *e-J Surf. Sci. Nanotechnol.* **2019,** *17*, 124. DOI: 10.1380/ejssnt.2019.124.

18. Vazirisereshk, M. R.; Martini, A.; Strubbe, D. A.; Baykara, M. Z., Solid Lubrication with MoS_2: A Review. *Lubricants* **2019,** *7* (7). DOI: 10.3390/lubricants7070057.

19. Kadantsev, E. S.; Hawrylak, P., Electronic Structure of a Single MoS_2 Monolayer. *Solid State Commun.* **2012,** *152* (10), 909. DOI: 10.1016/j.ssc.2012.02.005.

20. Gao, X.*, et al.*, Mechanical Properties and Thermal Conductivity of Graphene Reinforced Copper Matrix Composites. *Powder Techn.* **2016,** *301*, 601. DOI: 10.1016/j.powtec.2016.06.045.

21. Gao, X.*, et al.*, Tribological Properties of Copper Matrix Composites Reinforced with Homogeneously Dispersed Graphene Nanosheets. *J. Mater. Sci. Technol.* **2018,** *34* (10), 1925. DOI: 10.1016/j.jmst.2018.02.010.

22. Hou, K.*, et al.*, Construction of Highly Ordered Fluorinated Graphene Composite Coatings with Various Fluorine Contents for Enhanced Lubrication Performance. *Tribol. Lett.* **2015,** *60* (1), 6. DOI: 10.1007/s11249-015-0586-2.

23. Liu, Y.; Li, J.; Chen, X.; Luo, J., Fluorinated Graphene: A Promising Macroscale Solid Lubricant under Various Environments. *ACS Appl. Mater. Inter.* **2019,** *11* (43), 40470. DOI: 10.1021/acsami.9b13060.

24. Kwon, S.*, et al.*, Enhanced Nanoscale Friction on Fluorinated Graphene. *Nano Lett.* **2012,** *12* (12), 6043. DOI: 10.1021/nl204019k.

25. Matsumura, K.; Chiashi, S.; Maruyama, S.; Choi, J., Macroscale Tribological Properties of Fluorinated Graphene. *Appl. Surf. Sci.* **2018,** *432*, 190. DOI: 10.1016/j.apsusc.2017.06.190.

26. Lvova, N.; Annenkov, M., Methods of Synthesis and Physicochemical Properties of Fluorographenes. In *Handbook of Graphene Set*, **2019**; pp 63. 10.1002/9781119468455.ch3

27. Rosenkranz, A.; Liu, Y.; Yang, L.; Chen, L., 2D Nano-Materials Beyond Graphene: from Synthesis to Tribological Studies. *Appl. Nanosci.* **2020,** *10* (9), 3353. DOI: 10.1007/s13204-020-01466-z.

28. Kumar, R.; Hussainova, I.; Rahmani, R.; Antonov, M., Solid Lubrication at High-Temperatures - A Review. *Materials* **2022,** *15* (5), 1695. DOI: 10.3390/ma15051695.

29. Essa, F.*, et al.*, Enhancing the Tribological and Mechanical Properties of M50 Steel Using Solid Lubricants – A Detailed Review. *Proc. Inst. Mech. Eng.-J Sys.* **2018,** *232* (5), 619. DOI: 10.1177/1350650117723224.

30. Ajayi, O. O.*, et al.*, Boundary Film for Structural Ceramic Materials. *Wear* **1993,** *162-164*, 1150. DOI: 10.1016/0043-1648(93)90134-8.

31. Heymans, G.; Muñoz, A. I.; Mischler, S., Tribological Behaviour of Galvanic Gold Coatings Reinforced with Silica Nanoparticles. *Wear* **2020,** *462-463*, 203512. DOI: 10.1016/j.wear.2020.203512.

32. Moustafa, S. F.; El-Badry, S. A.; Sanad, A. M.; Kieback, B., Friction and Wear of Copper–Graphite Composites Made with Cu-Coated and Uncoated Graphite Powders. *Wear* **2002,** *253* (7), 699. DOI: 10.1016/S0043-1648(02)00038-8.

33. Zhao, H.; Liu, L.; Wu, Y.; Hu, W., Investigation on Wear and Corrosion Behavior of Cu–Graphite Composites Prepared by Electroforming. *Compos. Sci. Technol.* **2007,** *67* (6), 1210. DOI: 10.1016/j.compscitech.2006.05.013.

34. Futami, T.; Ohira, M.; Muto, H.; Sakai, M., Contact/Scratch-Induced Surface Deformation and Damage of Copper–Graphite Particulate Composites. *Carbon* **2009,** *47* (11), 2742. DOI: 10.1016/j.carbon.2009.05.034.

35. Bai, L.*, et al.*, Preparation and Properties of Copper-Plated Expanded Graphite/Copper Composites. *Tribol. Int.* **2021,** *161*, 107094. DOI: 10.1016/j.triboint.2021.107094.

36. Hwang, J., *et al.*, Enhanced Mechanical Properties of Graphene/Copper Nanocomposites Using a Molecular-Level Mixing Process. *Adv. Mater.* **2013,** *25* (46), 6724. DOI: 10.1002/adma.201302495.

37. Wang, L., *et al.*, High Apparent Strengthening Efficiency for Reduced Graphene Oxide in Copper Matrix Composites Produced by Molecule-Lever Mixing and High-Shear Mixing. *RSC Adv.* **2015,** *5* (63), 51193. DOI: 10.1039/C5RA04782J.

38. Zhang, X., *et al.*, Preparation and Characterization of Reduced Graphene Oxide/Copper Composites Incorporated with Nano-SiO_2 Particles. *J. Alloy. Comp.* **2016,** *671*, 465. DOI: 10.1016/j.jallcom.2016.02.068.

39. Yang, M., *et al.*, Simultaneously Enhancing the Strength, Ductility and Conductivity of Copper Matrix Composites with Graphene Nanoribbons. *Carbon* **2017,** *118*, 250. DOI: 10.1016/j.carbon.2017.03.055.

40. Yue, H., *et al.*, Effect of Ball-Milling and Graphene Contents on the Mechanical Properties and Fracture Mechanisms of Graphene Nanosheets Reinforced Copper Matrix Composites. *J. Alloy. Comp.* **2017,** *691*, 755. DOI: 10.1016/j.jallcom.2016.08.303.

41. Mai, Y. J., *et al.*, Surfactant-Free Electrodeposition of Reduced Graphene Oxide/Copper Composite Coatings with Enhanced Wear Resistance. *Appl. Surf. Sci.* **2018,** *433*, 232. DOI: 10.1016/j.apsusc.2017.10.014.

42. Hidalgo-Manrique, P., *et al.*, Copper/Graphene Composites: A Review. *J. Mater. Sci.* **2019,** *54* (19), 12236. DOI: 10.1007/s10853-019-03703-5.

43. Hynes Navasingh, R. J., *et al.*, 6 - Graphene-Based Nano Metal Matrix Composites: A Review. In *Nanocarbon and its Composites*, Khan, A.; Jawaid, M.; Inamuddin; Asiri, A. M., Eds. Woodhead Publishing: **2019**; pp 153. 10.1016/B978-0-08-102509-3.00006-7

44. Jia, Z., *et al.*, Synthesis, Characterization and Tribological Properties of Cu/Reduced Graphene Oxide Composites. *Tribol. Int.* **2015,** *88*, 17. DOI: 10.1016/j.triboint.2015.02.028.

45. Li, J.-f.; Zhang, L.; Xiao, J.-k.; Zhou, K.-c., Sliding Wear Behavior of Copper-Based Composites Reinforced with Graphene Nanosheets and Graphite. *Trans. Nonferr. Metal Soc.* **2015,** *25* (10), 3354. DOI: 10.1016/S1003-6326(15)63970-X.

46. Ci, X.*, et al.*, Revealing the Lubrication Mechanism of Fluorographene Nanosheets Enhanced GTL-8 Based Nanolubricant Oil. *Tribol. Int.* **2019,** *138*, 174. DOI: 10.1016/j.triboint.2019.05.044.

47. Zhao, W.; Ci, X., TiO_2 Nanoparticle/Fluorinated Reduced Graphene Oxide Nanosheet Composites for Lubrication and Wear Resistance. *ACS Appl. Nanomat.* **2020,** *3* (9), 8732. DOI: 10.1021/acsanm.0c01547.

48. Gu, W. C.*, et al.*, Synergistic Effects of 3D Porous Graphene and T161 As Hybrid Lubricant Additives on 316 ASS Surface. *Tribol. Int.* **2021,** *161*. DOI: 10.1016/j.triboint.2021.107072.

49. Li, S.*, et al.*, Synergistic Lubricating Performance of h-BN/GF Nanoparticles as Oil Additives for Steel-Steel Contact. *J. Tribol.- Trans. ASME* **2022,** *144* (6). DOI: 10.1115/1.4053033.

50. Li, W.*, et al.*, Investigating the Fluorination Degree of FG Nanosheets on the Tribological Properties of FG/PI Composite Coatings. *Prog. Org. Coat.* **2020,** *139*, 105481. DOI: 10.1016/j.porgcoat.2019.105481.

51. Zhou, S. G.*, et al.*, Tribological Behaviors of Polyimide Composite Coatings Containing Carbon Nanotubes and Fluorinated Graphene with Hybrid Phase or Blend Phase. *Prog. Org. Coat.* **2020,** *147*. DOI: 10.1016/j.porgcoat.2020.105800.

52. Liang, L.*, et al.*, Tribological Properties of Polytetrafluoroethylene Improved by Incorporation of Fluorinated Graphene with Various Fluorine/Carbon Ratios Under Dry Sliding Condition. *Tribol. Lett.* **2021,** *69* (1), 21. DOI: 10.1007/s11249-020-01398-3.

53. Liao, F., *et al.*, Surface Fluorinated Nickel-Graphene Nanocomposites for High-Efficiency Methanol Electrooxidation. *Int. J. Hydrogen Energ.* **2021,** *46* (53), 27138. DOI: 10.1016/j.ijhydene.2021.05.178.

54. Shan, Q., *et al.*, Interconnected 3D Fluorinated Graphene Host Enables an Ultrastable Lithium Metal Anode. *New J. Chem.* **2022,** *46* (19), 8981. DOI: 10.1039/D2NJ00432A.

55. Grandin, M.; Wiklund, U., Friction, Wear and Tribofilm Formation on Electrical Contact Materials in Reciprocating Sliding Against Silver-Graphite. *Wear* **2013,** *302* (1), 1481. DOI: 10.1016/j.wear.2013.02.007.

56. Zhou, W., *et al.*, Preparation of a C/C–Cu composite with Mo_2C coatings as a modification interlayer. *Mater. Lett.* **2015,** *145*, 264. DOI: 10.1016/j.matlet.2015.01.111.

57. Hutchings, I.; Shipway, P., 5 - Sliding Wear. In *Tribology (Second Edition)*, Hutchings, I.; Shipway, P., Eds. Butterworth-Heinemann: **2017**; pp 107. 10.1016/B978-0-08-100910-9.00005-2

58. Kamimoto, Y., *et al.*, Nickel–Carbon Composite Plating Using a Watts Nickel Electroplating Bath. *SN Appl. Sci.* **2020,** *2* (2), 170. DOI: 10.1007/s42452-020-1991-1.

59. Gan, Y. X., Electrolytic Metallic Coatings for Carbon Fibers. *Mater. Manuf. Process.* **1994,** *9* (2), 263. DOI: 10.1080/10426919408934903.

60. Mandal, A., *et al.*, Tribological Behavior of Graphene-Reinforced 316L Stainless-Steel Composite Prepared *via* Selective Laser Melting. *Tribol. Int.* **2020,** *151*, 106525. DOI: 10.1016/j.triboint.2020.106525.

61. Wan, S. H., Solid Lubricant: Soft Metal. In *Encyclopedia of Tribology*, Wang, Q. J.; Chung, Y.-W., Eds. Springer US: Boston, MA, **2013**; pp 3152. 10.1007/978-0-387-92897-5_1231

62. Fan, K., *et al.*, Toward Excellent Tribological Performance as Oil-Based Lubricant Additive: Particular Tribological Behavior of Fluorinated Graphene. *ACS Appl. Mater. Inter.* **2018,** *10* (34), 28828. DOI: 10.1021/acsami.8b07635.

63. Lin, L., *et al.*, Formation of Tunable Graphene Oxide Coating with High Adhesion. *Phys. Chem. Chem. Phys.* **2016,** *18* (7), 5086. DOI: 10.1039/C5CP06906H.

64. Onodera, T., *et al.*, Transfer-Film Formation Mechanism of Polytetrafluoroethylene: A Computational Chemistry Approach. *J. Phys. Chem. C* **2013,** *117* (20), 10464. DOI: 10.1021/jp400515j.

Supporting Information

Enhanced tribological properties of copper metal-matrix composites reinforced with fluorinated graphene oxide nanosheets

Nicky Savjani, Vicente Orts Mercadillo, Darren Hodgeman, Yubao Deng, Cristina Vallés, Mark A. Bissett and Ian A. Kinloch**

GO and FGO powder characterisation

Characterization of the GO and FGO powders was carried out using a variety of techniques. Transmission electron microscopy (TEM) was performed using a Tecnai T20 scope. Samples were prepared by drop casting dispersions of 0.1 mg/ml (F)GO in 1:1 water, IPA onto a lacey carbon support. SEM was carried out using a Zeiss Ultra 55 FEG scope. Samples were prepared by drop casting dispersion of 1 mg/ml (F)GO in 1:1 water, IPA onto a silicon wafer support. Contact angle measurements were taken on a Biolin Scientific, Theta Lite optical tensiometer. A 2 mL water droplet was pipetted onto the pelletized powder (13mm discs, consisting of 0.5g of powder, pressed at 10 tons for 5 minutes using a hydraulic press). Laser diffraction particle sizing was carried out using a Malvern Mastersizer, with the HydroEV attachment. Samples were dispersed in 1:1 water, IPA solution until appropriate obscuration values were reached and measured post two rounds of 120s sonication. Bulk FTIR spectra were obtained from 32 co-averages collected in transmission mode using an ATR-FTIR spectrometer (Nicolet iS50 spectrometer, Thermo Scientific) with a diamond crystal window, operating at 1 cm^{-1} resolution across a 650-4000 cm^{-1} range. Raman Spectroscopy was carried out on a Renishaw InVia with a 532 nm laser and a 50x scope. The StreamHR mapping function was used to map 480 spectra over a ~2000 μm^2 area.

X-ray Photoelectron Spectroscopy (XPS) was performed on an Axis Ultra Hybrid spectrometer (Kratos Analytical) using monochromated Al Kα radiation (1486.6 eV, 10 mA emission at 150 W, spot size 300 x 700 μm) with a base vacuum pressure of $\sim 5 \times 10^{-9}$ mbar. Charge neutralization was achieved using a filament. Analysis was carried out in CasaXPS.[1] Binding energy scale calibration was performed using C-C in the C 1s photoelectron peak at 284.7 eV. The high-resolution (HR) C_{1s} peaks were fitted using a finite Lorentzian (LF) peak shape, with a damping parameter used to quash the peak tail.[2] A three-parameter Tougaard background (U 3) was used and other component peaks were modelled as symmetric Voigt line shapes LA(1,600), with a consistent FWHM. The number of component peaks was initially approximated by eye and refined in subsequent fittings to achieve a random residual distribution. A Shirley background and symmetric Voigt components of equal FWHM were used to deconvolute HR-O_{1s}. A three-parameter Tougaard background and symmetric Voigt components of equal FWHM were used to deconvolute HR-F_{1s}. The transitions with the largest peak areas were selected for quantification. In the case of Cu_{2p}, K_{2p} and P_{2p}, the doublet pairs were used and scaled using the total relative sensitivity factor (RSF).[1] The K_{2p} doublet overlaps with the C_{1s} peak, as such a synthetic peak model was fitted to apportion the area.[1] Since K_{2p} spin-orbit splitting gives rise to a doublet, the component areas of 1/2 and 3/2 are constrained to a ratio of 0.5.

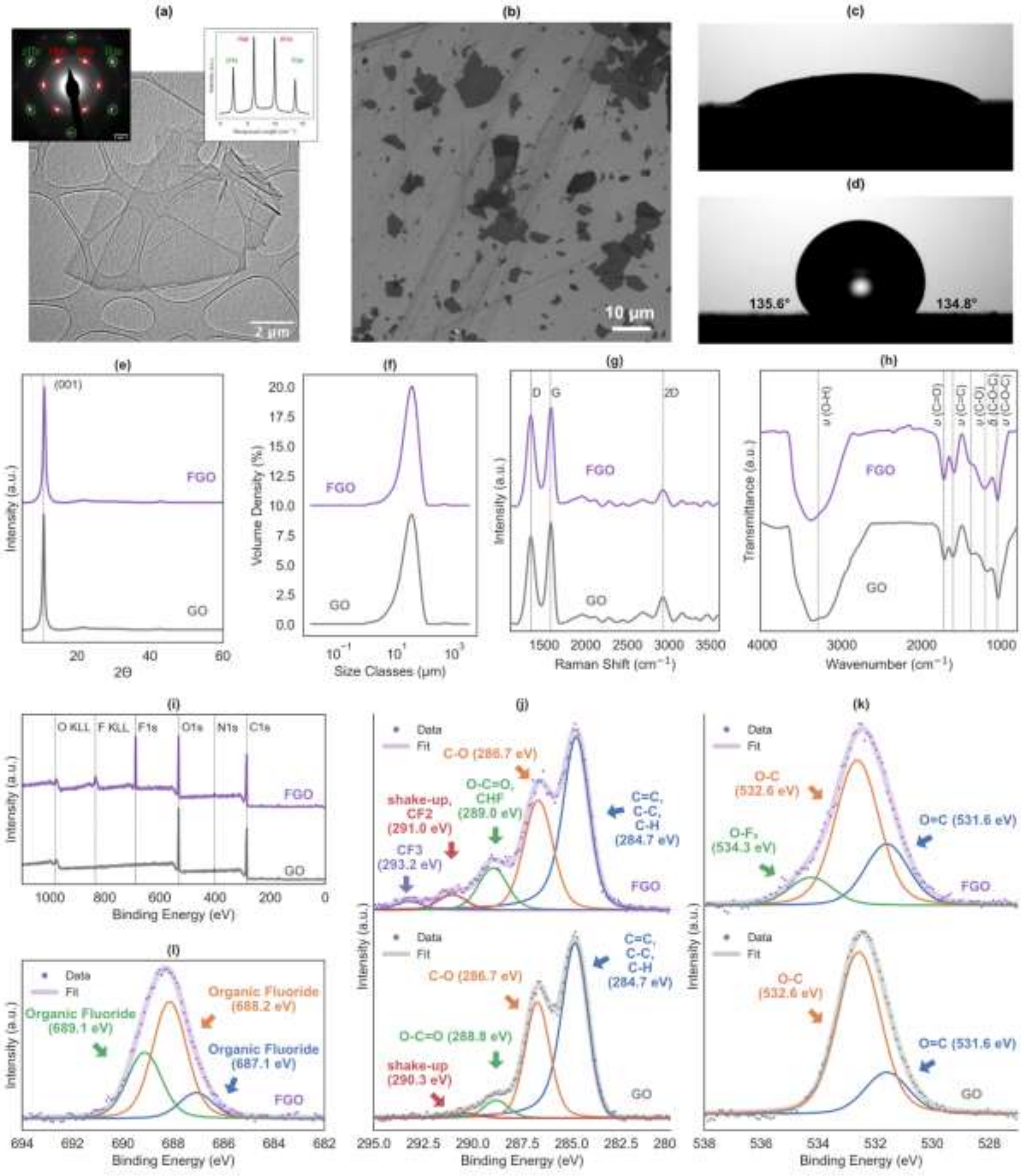

Figure S1. (a) TEM image of a GO flake on a lacey carbon support and its selected area electron diffraction pattern (inset top left) and accompanying intensity profile (inset top right). SEM of an image of GO sheets drop-cast onto a silicon wafer. (c, d) GO and FGO contact angle measurement stills. (e-h) Characterisation of GO and FGO using XRD, laser-diffraction particle sizing, Raman spectroscopy, and FTIR. (i) XPS Survey scan for GO and FGO. (j-l) High-resolution C_{1s}, O_{1s} and F_{1s} XPS scans for GO and FGO.

The detailed characterization of FGO and GO powders is summarized in Figure S1. A TEM image of a typical GO flake is shown in (a), its transparent nature indicating few-layer material, the inset (top left) selected area electron diffraction pattern (SAED), taken at the center of the flake shows a hexagonal pattern of spots (annotated with Miller-Bravais *hkil* notation) extending across the captured image. The linear intensity profile of the SAED pattern in the inset (top right), shows that the intensity ratio between 1100 and 2110 is 1.7, this is consistent with few-layer behaviour[3] and follows literature values for GO.[4] No diffraction spots from the oxygen moieties are seen, as expected since these do not produce the requisite ordered lattice arrays.[4]

The distribution of lateral size can be visualized in the SEM image of GO flakes drop cast onto a silicon wafer in (b). The consistent contrast indicates flakes of similar thickness, while a range of flake sizes can be observed from < 1 µm, to > 10 µm. The particle size distribution in (f) shows an asymmetric distribution for GO and FGO, as the blended freeze-dried powder had been sieved to < 50 µm, to minimize the presence of agglomerates. The D_{50} is 28.5 and 30.5 µm for GO and FGO respectively. The slight increase could be indicated by larger aggregates in the FGO, possibly due to worse dispersion in the water and IPA solution due to the presence of hydrophobic fluorine groups. The characteristic (001) peak can be observed for both GO (at 10.9°) and FGO (at 11.0°) in the XRD spectra in (e), from which the interlayer spacing is calculated to be 8.1 and 8.0 Å respectively, suggesting that there is minimal effect on sheet-stacking post-fluorination.

The effect of fluorination can be most clearly observed in contact angle measurements, as shown in (c, d) for GO and FGO respectively. For the former, the hydrophilic surface leads the water to spread across the field of view, and so the contact angle is too small to accurately measure. Whereas for the latter, significant hydrophobic behavior is observed due to the presence of fluorine groups increasing the contact angle to 135.2°.

The average FGO and GO spectra for the mapped area are shown in (g). Each spectrum shows a characteristic graphitic G mode at ~1566 cm^{-1} and defect-induced D mode at ~1342 cm^{-1} and weak 2D mode at ~2930 cm^{-1}. The I_D/I_G ratio increases from 0.93 (±0.02) for GO to 0.97 (±0.05) for FGO. However, since the FWHM of the G peaks is above 30 (61.2 and 56.8 cm^{-1} for GO and FGO respectively), the material is in the second stage of defect evolution, wherein an increase in I_D/I_G indicates a reduction in disorder.[5] Indicating that the plasma fluorination acts to clean the graphitic surface of amorphous debris and/or passivate defects. The (F)GO powders were analysed under ATR-FTIR, as shown in (h). Both materials share a similar spectrum, hydroxyl (-OH) groups display a broad peak of ~3400 cm^{-1}, while other carbon lattice and oxygen functionality-derived peaks, appear between 2000 – 1000 cm^{-1}. These consist of carboxylic stretching from C=O at 1720 cm^{-1} and C-OH at 1380 cm^{-1}[6], aromatic C=C stretching at 1610 cm^{-1} [7], and epoxy (C-O-C) deformations and stretching at 1200 and 1050 cm^{-1} respectively[8, 9]. Fluorination appears to slightly dampen both carboxylic and epoxy peaks, implying functionalisation occurs via the substitution of these oxygen moieties with fluorine.

Table S1: Relative atomic composition (at.%) of (F)GO powders.

Material	C_{1s}	O_{1s}	N_{1s}	F_{1s}
GO	76.6 (±0.4)	22.6 (±0.8)	0.8 (±1.2)	0.0
FGO	68.4 (±1.0)	20.2 (±0.5)	0.7 (±1.1)	10.8 (±0.9)

The XPS survey scans for the (F)GO powders in (i) show intense C_{1s}, O_{1s} and in the case of FGO, F_{1s} peaks, as well as a weak N_{1s} peak in both spectra. The relative atomic composition of each is summarised in Table S1. The increase in fluorine content comes primarily at the expense of 8.2 at.% carbon and 2.4 at.% oxygen suggesting that the fluorine is primarily passivating existing carbon defects or creating new ones, and only weakly displacing existing oxygen moieties.

The HR-C_{1s} (F)GO scans in (j) show a broad and asymmetric peak, due to the highly defective graphitic nature of the materials. This can be deconvoluted into a neutral carbon peak (C-C, C=C, C-H) at 284.7eV. For GO, three additional components were observed: C-O (286.7 eV), O-C=O (288.8 eV) and a shake-up feature (290.3 eV).[2] Assigning peaks in FGO powder is more complex as the fluorine chemical states overlap with existing oxygen-derived functionalities. CHF overlaps with the O-C=O peak at 289.0 eV, CF_2 overlaps with the shake-up at 291.0 eV, both of which broaden and increase in intensity, and a new CF_3 peak appears at 293.2 eV.[10] The HR-O_{1s} scans in (k) show two components for GO, a C=O peak (531.6 eV) and a C-O peak (532.6 eV).[11] These are present in FGO, alongside the O-F_x peak (534.3 eV).[12] Indicating, that fluorination occurs both through oxygen modalities and the carbon skeleton. The HR-F_{1s} for FGO in (l) can be deconvoluted into three component peaks centred between 687 – 689 eV assigned to organic fluorides.

GO and FGO copper-plating dispersion filtrate characterisation

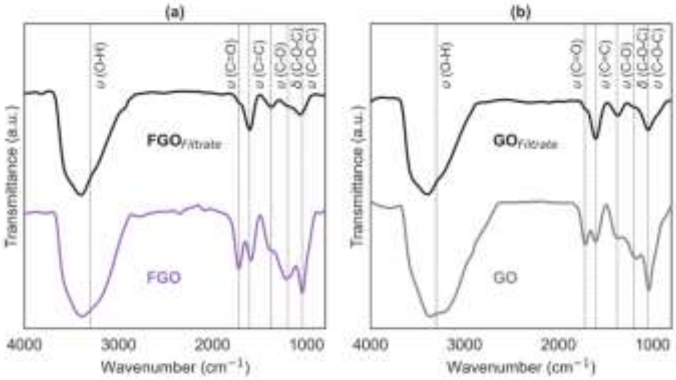

Figure S2: (a) FGO and (b) GO powder and corresponding copper plating dispersion filtrate.

Following the discovery of heterogeneous growth processes and increased nanosheet interlayer spacing in the **FGO-CMMC** and **GO-CMMC** coatings, the nature of the 2D materials within **(F)GO-Copper** plating dispersions was investigated further. Enabling a better understanding of the chemical modifications imposed on the (F)GO powders by combining them with the copper plating solutions. To do this, 2 mL aliquots of the 1 mg/mL **(F)GO-Copper** plating dispersions were extracted and diluted with 8 mL deionised water. The diluted solutions were passed through a PVDF filter via a syringe filtration assembly (13 mm diameter, 0.1 μm pore size, syringed at 10 mL/h), followed by two 10 mL DI water washes. The resulting filtrates (called $\mathbf{FGO_{Filtrate}}$ and $\mathbf{GO_{Filtrate}}$) were dried *via vacuo* for 4 hours at 40 °C before characterisation. The results shown are for material plated for 6 hours at 0.25 A/dm^2 and are representative of both un-plated filtrates and filtrates plated for 3 hours at 0.5 A/dm^2.

The ATR-FTIR spectra of the (**F**)$\mathbf{GO_{Filtrate}}$, have been plotted alongside the relevant powder in Figure S2 to better discern spectral changes. In both cases, the hydroxyl and aromatic C=C peaks are unaffected, however, the intensity of the other oxygen functionality peaks is dampened, in particular the carboxyl C=O (1720 cm^{-1}) peak. The lack of bands in the alkyl C-H region (2900-2750 cm^{-1}) eliminates organic functionalisation, suggesting this is due to carboxyl-edge functionalisation by an inorganic component.

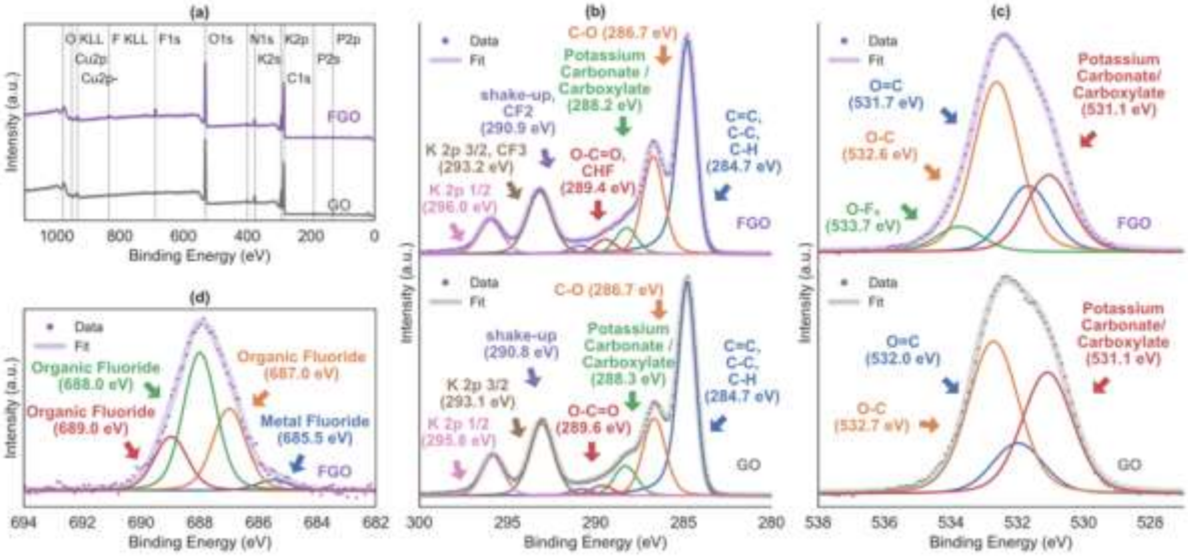

Figure S3: (a) XPS survey scan and (b-d) high-resolution C_{1s}, O_{1s} and F_{1s} scans for (F)GO$_{Filtrate}$ samples.

The XPS analysis for the **(F)GO$_{Filtrate}$** samples is summarised in Figure S3. The survey scans in (a) show the change in elemental composition post-dispersion: The presence of copper, potassium and phosphorous peaks is expected as these are contained in the bath mixture. The relative atomic composition of each is summarised in Table S2. The potassium is present in larger quantities (4.9 and 4.2 at. % for **GO$_{Filtrate}$** and **FGO$_{Filtrate}$**) than copper or phosphorus, indicative of favoured potassium-functionalisation on the (F)GO nanosheets. The drop in relative fluorine content in the FGO post-dispersion (-8.7 at.%) suggests that fluorine groups are being displaced.

Table S2: Relative atomic composition (at.%) of (F)GO copper-plating dispersion filtrate.

Material	C_{1s}	O_{1s}	N_{1s}	F_{1s}	K_{2p}	Cu_{2p}	P_{2p}
GO$_{Filtrate}$	68.2 (±0.2)	24.7 (±0.1)	1.0 (±0.1)	0.0	4.9 (±0.1)	0.8 (±0.04)	0.4 (±0.1)
FGO$_{Filtrate}$	69.1 (±0.5)	23.5 (±0.2)	0.7 (±0.1)	1.9 (±0.4)	4.2 (±0.03)	0.5 (±0.05)	0.2 (±0.07)

The HR-C_{1s} peak for the **(F)GO$_{\textbf{Filtrate}}$** samples overlaps with K_{2p} peaks so both have been fitted simultaneously in (b). A new peak appears at ~288.2 eV assigned which can be assigned to C_{1s} signals for potassium carbonate/carboxylate, further evidencing functionalisation with the potassium metal in dispersion.[13] The shake-up, CF_2 and O-C=O, CHF peaks have a higher relative area in the FGO scan, which could be attributed to any fluorine that remains post-deposition. The HR-O_{1s} peak for the **(F)GO$_{\textbf{Filtrate}}$** samples, shown in (c), broadens towards lower binding energies, to encompass a potassium carbonate/carboxylate peak (~ 531 eV). The O-F_x peak weakens in the FGO post-deposition, in line with the drop in atomic fluorine concentration. In the HR-F_{1s} peak for **FGO$_{\textbf{Filtrate}}$**, shown in (d), a new peak appears at 685.5 eV, indicating the presence of metallic fluoride bonds.[14] This suggests that the displaced fluorine groups may go on to react with potassium ions in solution and filter out as salts on the **FGO$_{\textbf{Filtrate}}$**.

GO-CMMC and Cu_{Ref} coating characterisation

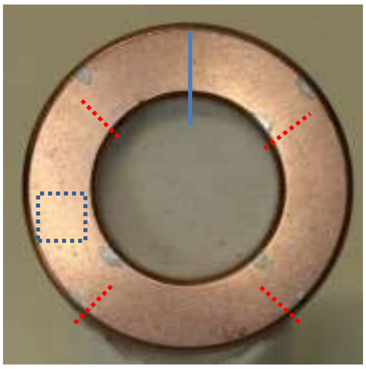

Figure S4. Photograph of a representative CMMC. The samples were orientated in the same manner before measurement (the point where each sample was hung is indicated by the blue solid line). Before deposition, latex masks were applied at 8 locations to inhibit deposition for coating thickness determination. The thicknesses were measured across the four lines in red and averaged. The blue box denotes the 9mm^2 section where the roughness was analysed in each sample by white light interferometry.

Cu_{Ref} coatings typically showed good uniformity (Figure S6c, d, g, h, k, and l) and thicknesses close to the ascribed 20 μm target (Figure S5). White light interferometry showed that **$Cu_{Ref(0.25CD)}$** and **$Cu_{Ref(0.5CD)}$** coatings are deposited uniformity across the whole substrate with R_a values of between 0.2 and 0.3 μm, consistent with the roughness of the underlying substrate (~0.25 μm).

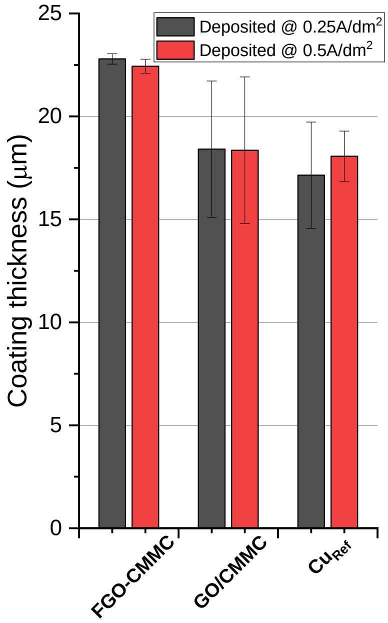

Figure S5. The measured thicknesses of FGO-CMMC, GO-CMMC and Cu$_{Ref}$ coatings. The values are based on the average thickness measured across each of the paired masked areas.

GO-CMMC coatings show a similar coating structure as **FGO-CMMCs**; a slight visual roughening of the surface with evidence of misaligned growths on the surface. SEM and WL interferometry imaging shows that the density of growths in GO-CMMCs is significantly lower, but comprises larger grains (Figure S6 a, b, e, f). SEM imaging of **GO-CMMCs** (Figure S6i, j) coatings reveals that GO nanosheets are embedded and protruding from the core of the misorientated grains, with no copper nanoparticle growth on its surface,

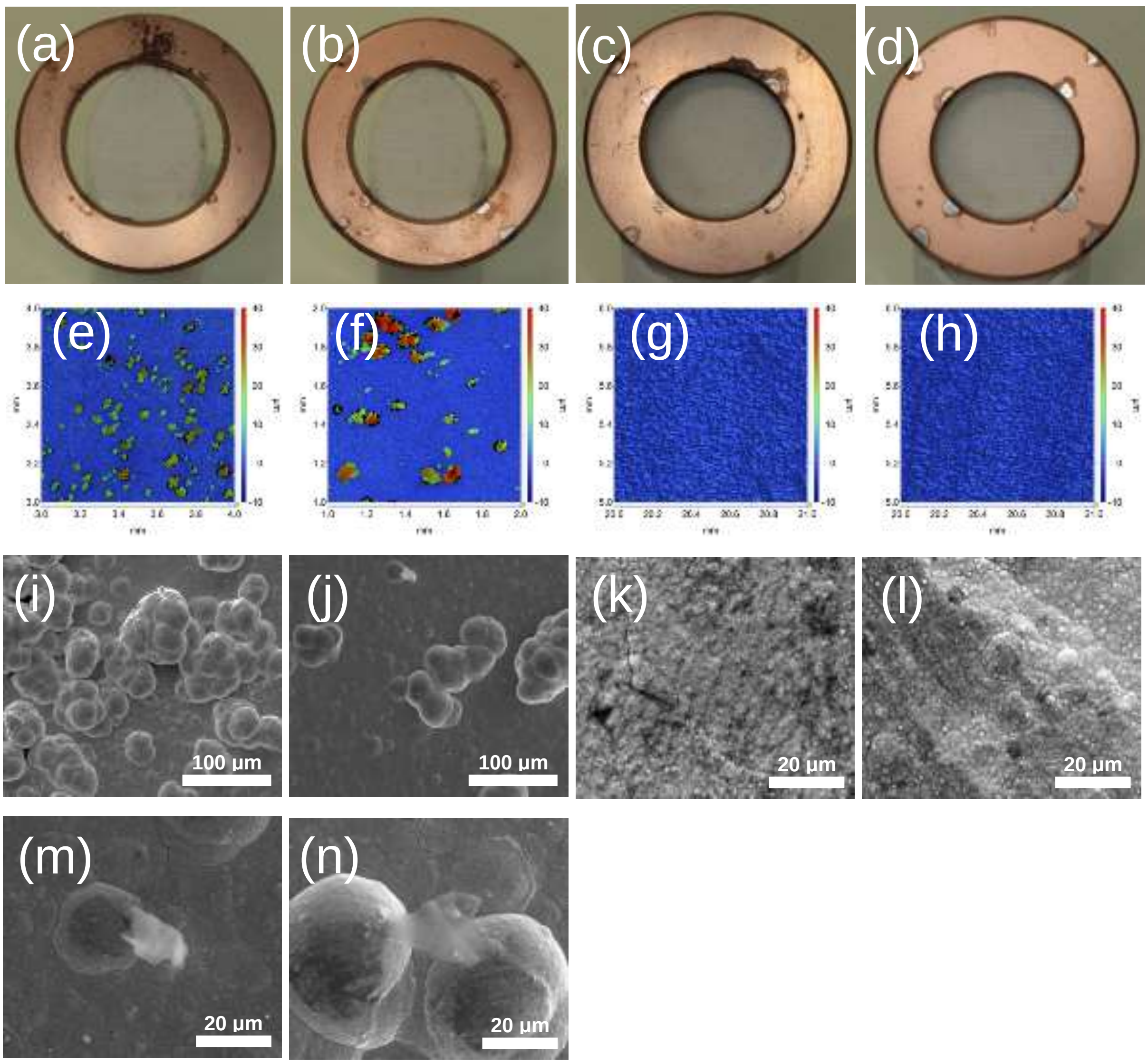

Figure S6. Optical (a-d), White-light interferometry (e-f) and electron microscopy (g-n) images of the GO-CMMC and Cu$_{Ref}$ coatings electrodeposited onto AISI 52100 steel: (a, e, i and m) GO-CMMC$_{(0.25CD)}$ (b, f, j and n) GO-CMMC$_{(0.5CD)}$, (c, g and k) Cu$_{Ref(0.25CD)}$, (d, h and l) Cu$_{Ref(0.5CD)}$.

Table S3. Statistical analysis from the topographical data of the FGO-CMMC and GO-CMMC coatings. All measurements were carried out from a 3.75 mm^2 area of each coating.

Coating	**Number of growths**	**Coverage of growths (% area)**	**Average growth height (μm)**	**Avg. surface area per growth (mm^2)**	**Roughness (μm)**
FGO-CMMC$_{(0.25CD)}$	2007	51.0	12.8 (± 4.4)	0.0036 (± 0.006)	2.8
FGO-CMMC$_{(0.5CD)}$	2005	41.0	17.5 (± 5.9)	0.0029 (± 0.003)	3.1
GO-CMMC$_{(0.25CD)}$	299	9.9	36.0 (± 9.2)	0.0046 (± 0.005)	2.6
GO-CMMC$_{(0.5CD)}$	297	10.9	32.8 (± 9.2)	0.0051 (± 0.006)	1.2

Post-wear analysis on GO-CMMC and $\mathrm{Cu_{Ref}}$ coatings

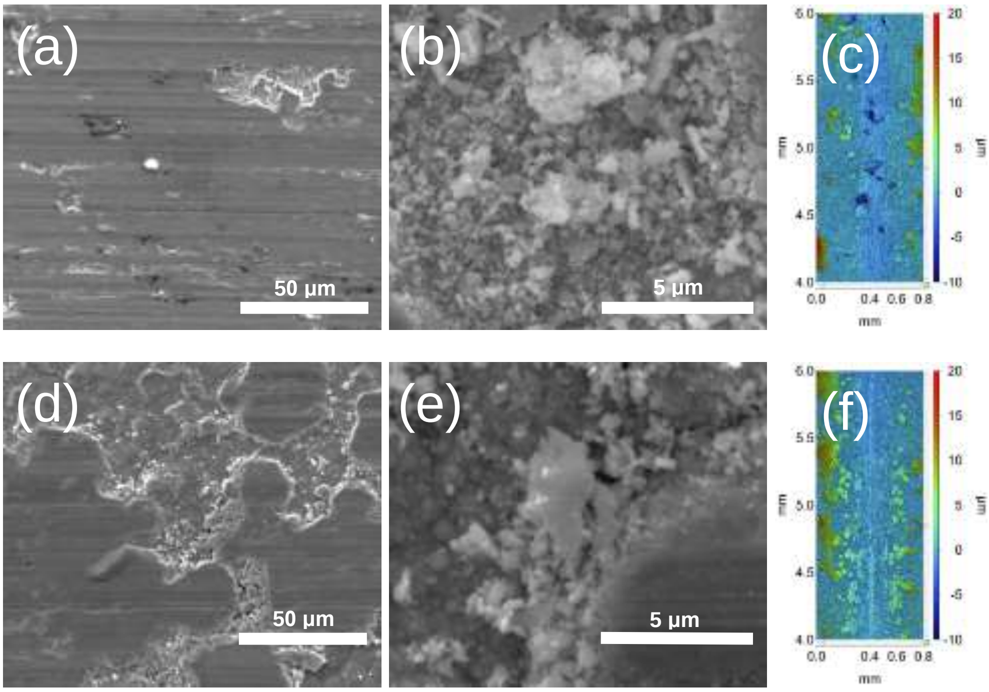

Figure S7. SEM and WL interferometry imaging of the wear scars on the sliding tracks of GO-CMMC coatings. The wear scars on (a-c) GO-$\mathrm{CMMC_{(0.25CD)}}$ and (d-f) GO-$\mathrm{CMMC_{(0.5CD)}}$.

Figure S8. (a) SEM imaging and (b, c) EDX mapping of a wear surface formed on GO-CMMC(0.25CD) after PoD sliding for 10,000 revs. (d) An SEM image of the wear surface on the AISI 52100 counterface ball after PoD sliding on GO-CMMC$_{(0.25CD)}$, (e-g) accompanied by elemental maps obtained by EDX analysis

References

1. Walton, J.; Wincott, P.; Fairley, N.; Carrick, A., *Peak Fitting with CasaXPS*. Accolyte Science: Knutsford, UK, 2010.

2. Gengenbach, T. R.; Major, G. H.; Linford, M. R.; Easton, C. D., Practical Guides for X-Ray Photoelectron Spectroscopy (XPS): Interpreting the Carbon 1s Spectrum. *J. Vac. Sci. Techn. Vac. Surf. Films* **2021,** *39* (1), 013204. DOI: 10.1116/6.0000682.

3. Meyer, J. C*., et al.*, On the Roughness of Single- and Bi-Layer Graphene Membranes. *Solid State Commun.* **2007,** *143* (1-2), 101. DOI: 10.1016/j.ssc.2007.02.047.

4. Wilson, N. R*., et al.*, Graphene Oxide: Structural Analysis and Application as a Highly Transparent Support for Electron Microscopy. *Acs Nano* **2009,** *3* (9), 2547. DOI: 10.1021/nn900694t.

5. Nagyte, V*., et al.*, Raman Fingerprints of Graphene Produced by Anodic Electrochemical Exfoliation. *Nano Lett.* **2020,** *20* (5), 3411. DOI: 10.1021/acs.nanolett.0c00332.

6. Lee, D. W*., et al.*, The Structure of Graphite Oxide: Investigation of Its Surface Chemical Groups. *J. Phys. Chem. B* **2010,** *114* (17), 5723. DOI: 10.1021/jp1002275.

7. Ţucureanu, V.; Matei, A.; Avram, A. M., FTIR Spectroscopy for Carbon Family Study. *Crit. Rev. Anal. Chem.* **2016,** *46* (6), 1. DOI: 10.1080/10408347.2016.1157013.

8. Johra, F. T.; Jung, W.-G., Hydrothermally Reduced Graphene Oxide as a Supercapacitor. *Appl. Surf. Sci.* **2015,** *357*, 1911. DOI: 10.1016/j.apsusc.2015.09.128.

9. Díez-Pascual, A. M.; Díez-Vicente, A. L., Poly(propylene fumarate)/Polyethylene Glycol-Modified Graphene Oxide Nanocomposites for Tissue Engineering. *ACS Appl. Mater. Inter.* **2016,** *8* (28), 17902. DOI: 10.1021/acsami.6b05635.

10. Wanger, C. D*., et al.*, *Handbook of X-ray Photoelectron Spectroscopy* Perkin-Elmer Corp., Physical Electronics Division: Eden Prairie, Minnesota, USA, 1979. 10.1002/sia.740030412

11. Wagner, C. D., *The NIST X-Ray Photoelectron Spectroscopy (XPS) Database*. U.S. Dept. of Commerce, National Institute of Standards and Technology: Gaithersburg, MD, USA, 1991.

12. ThermoFisher Oxygen X-ray photoelectron spectra. https://www.thermofisher.com/uk/en/home/materials-science/learning-center/periodic-table/non-metal/oxygen.html (accessed 8th June 2022).

13. Shchukarev, A. V.; Korolkov, D. V., XPS Study of group IA carbonates. *Cent. Eur. J. Chem.* **2004,** *2* (2), 347. DOI: 10.2478/bf02475578.

14. ThermoFisher Fluorine X-ray photoelectron spectra. https://www.thermofisher.com/uk/en/home/materials-science/learning-center/periodic-table/halogen/fluorine.html (accessed 8th June 2022).